Wavefront sensorless adaptive optics OCT with the DONE algorithm for *in vivo* human retinal imaging [Invited]

HANS R. G. W. VERSTRAETE,[1,*] MORGAN HEISLER,[2] MYEONG JIN JU,[2] DANIEL WAHL,[2] LAURENS BLIEK,[1] JEROEN KALKMAN,[3] STEFANO BONORA,[3] YIFAN JIAN,[2,5,6] MICHEL VERHAEGEN,[1,5] AND MARINKO V. SARUNIC[2,5]

[1]*Delft Center for Systems and Control, Delft University of Technology, Mekelweg 2, 2628 CD, Delft, The Netherlands*
[2]*School of Engineering Science, Simon Fraser University, 8888 University Drive, Burnaby, BC, V5A 1S6, Canada*
[3]*Department of Imaging Physics, Delft University of Technology, Lorentzweg 1, 2628 CJ, Delft, The Netherlands*
[4]*CNR-Institute of Photonics and Nanotechnology, via Trasea 7, Padova, Italy*
[5]*These authors contributed equally*
[6]*yjian@sfu.ca*
[*]*h.r.g.w.verstraete@tudelft.nl*

Abstract: In this report, which is an international collaboration of OCT, adaptive optics, and control research, we demonstrate the data-based online nonlinear extremum-seeker (DONE) algorithm to guide the image based optimization for wavefront sensorless adaptive optics (WFSL-AO) OCT for *in vivo* human retinal imaging. The ocular aberrations were corrected using a multi-actuator adaptive lens after linearization of the hysteresis in the piezoelectric actuators. The DONE algorithm succeeded in drastically improving image quality and the OCT signal intensity, up to a factor seven, while achieving a computational time of 1 ms per iteration, making it applicable for many high speed applications. We demonstrate the correction of five aberrations using 70 iterations of the DONE algorithm performed over 2.8 s of continuous volumetric OCT acquisition. Data acquired from an imaging phantom and *in vivo* from human research volunteers are presented.

References and links

1. D. Huang, E. Swanson, C. Lin, J. Schuman, W. Stinson, W. Chang, M. Hee, T. Flotte, K. Gregory, C. Puliafito, and J. Fujimoto, "Optical coherence tomography," Science **254**, 1178–1181 (1991).
2. M. Pircher, B. Baumann, E. Götzinger, and C. K. Hitzenberger, "Retinal cone mosaic imaged with transverse scanning optical coherence tomography," Opt. Lett. **31**, 1821–1823 (2006).
3. B. Potsaid, I. Gorczynska, V. J. Srinivasan, Y. Chen, J. Jiang, A. Cable, and J. G. Fujimoto, "Ultrahigh speed spectral / Fourier domain OCT ophthalmic imaging at 70,000 to 312,500 axial scans per second," Opt. Express **16**, 15149–15169 (2008).
4. M. Pircher, E. Götzinger, H. Sattmann, R. A. Leitgeb, and C. K. Hitzenberger, "In vivo investigation of human cone photoreceptors with SLO/OCT in combination with 3D motion correction on a cellular level," Opt. Express **18**, 13935–13944 (2010).
5. D. R. Williams, "Imaging single cells in the living retina," Vision Res. **51**, 1379–1396 (2011).
6. Y. Zhang, J. Rha, R. S. Jonnal, and D. T. Miller, "Adaptive optics parallel spectral domain optical coherence tomography for imaging the living retina," Opt. Express **13**, 4792–4811 (2005).
7. R. J. Zawadzki, S. M. Jones, S. S. Olivier, M. Zhao, B. A. Bower, J. A. Izatt, S. Choi, S. Laut, and J. S. Werner, "Adaptive-optics optical coherence tomography for high-resolution and high-speed 3d retinal in vivo imaging," Opt. Express **13**, 8532–8546 (2005).
8. Y. Zhang, B. Cense, J. Rha, R. S. Jonnal, W. Gao, R. J. Zawadzki, J. S. Werner, S. Jones, S. Olivier, and D. T. Miller, "High-speed volumetric imaging of cone photoreceptors with adaptive optics spectral-domain optical coherence tomography," Opt. Express **14**, 4380–4394 (2006).

9. B. Cense, E. Koperda, J. M. Brown, O. P. Kocaoglu, W. Gao, R. S. Jonnal, and D. T. Miller, "Volumetric retinal imaging with ultrahigh-resolution spectral-domain optical coherence tomography and adaptive optics using two broadband light sources," Opt. Express **17**, 4095–4111 (2009).

10. K. Kurokawa, K. Sasaki, S. Makita, M. Yamanari, B. Cense, and Y. Yasuno, "Simultaneous high-resolution retinal imaging and high-penetration choroidal imaging by one-micrometer adaptive optics optical coherence tomography," Opt. Express **18**, 8515–8527 (2010).

11. O. P. Kocaoglu, S. Lee, R. S. Jonnal, Q. Wang, A. E. Herde, J. C. Derby, W. Gao, and D. T. Miller, "Imaging cone photoreceptors in three dimensions and in time using ultrahigh resolution optical coherence tomography with adaptive optics," Biomed. Opt. Express **2**, 748–763 (2011).

12. F. Felberer, J.-S. Kroisamer, B. Baumann, S. Zotter, U. Schmidt-Erfurth, C. K. Hitzenberger, and M. Pircher, "Adaptive optics SLO/OCT for 3D imaging of human photoreceptors in vivo," Biomed. Opt. Express **5**, 439–456 (2014).

13. Y. N. Sulai and A. Dubra, "Non-common path aberration correction in an adaptive optics scanning ophthalmoscope," Biomed. Opt. Express **5**, 3059–3073 (2014).

14. M. A. Vorontsov, "Decoupled stochastic parallel gradient descent optimization for adaptive optics: integrated approach for wave-front sensor information fusion," J. Opt. Soc. Am. A **19**, 356–368 (2002).

15. J. R. Fienup and J. J. Miller, "Aberration correction by maximizing generalized sharpness metrics," J. Opt. Soc. Am. A **20**, 609–620 (2003).

16. S. Zommer, E. N. Ribak, S. G. Lipson, and J. Adler, "Simulated annealing in ocular adaptive optics," Opt. Lett. **31**, 939–941 (2006).

17. D. Débarre, E. J. Botcherby, T. Watanabe, S. Srinivas, M. J. Booth, and T. Wilson, "Image-based adaptive optics for two-photon microscopy," Opt. Lett. **34**, 2495–2497 (2009).

18. H. Yang, O. Soloviev, and M. Verhaegen, "Model-based wavefront sensorless adaptive optics system for large aberrations and extended objects," Opt. Express **23**, 24587–24601 (2015).

19. H. Hofer, N. Sredar, H. Queener, C. Li, and J. Porter, "Wavefront sensorless adaptive optics ophthalmoscopy in the human eye," Opt. Express **19**, 14160–14171 (2011).

20. D. J. Wahl, Y. Jian, S. Bonora, R. J. Zawadzki, and M. V. Sarunic, "Wavefront sensorless adaptive optics fluorescence biomicroscope for in vivo retinal imaging in mice," Biomed. Opt. Express **7**, 1–12 (2016).

21. M.-R. Nasiri-Avanaki, S. Hojjatoleslami, H. Paun, S. Tuohy, A. Meadway, G. Dobre, and A. Podoleanu, "Optical coherence tomography system optimization using simulated annealing algorithm," Proceedings of Mathematical Methods and Applied Computing, WSEAS pp. 669–674 (2009).

22. S. Bonora and R. J. Zawadzki, "Wavefront sensorless modal deformable mirror correction in adaptive optics: optical coherence tomography," Opt. Lett. **38**, 4801–4804 (2013).

23. H. R. G. W. Verstraete, B. Cense, R. Bilderbeek, M. Verhaegen, and J. Kalkman, "Towards model-based adaptive optics optical coherence tomography," Opt. Express **22**, 32406–32418 (2014).

24. Y. Jian, J. Xu, M. A. Gradowski, S. Bonora, R. J. Zawadzki, and M. V. Sarunic, "Wavefront sensorless adaptive optics optical coherence tomography for in vivo retinal imaging in mice," Biomed. Opt. Express **5**, 547–559 (2014).

25. S. Bonora, Y. Jian, P. Zhang, A. Zam, E. N. Pugh, R. J. Zawadzki, and M. V. Sarunic, "Wavefront correction and high-resolution in vivo OCT imaging with an objective integrated multi-actuator adaptive lens," Opt. Express **23**, 21931–21941 (2015).

26. Y. Jian, R. J. Zawadzki, and M. V. Sarunic, "Adaptive optics optical coherence tomography for in vivo mouse retinal imaging," J. Biomed. Opt. **18**, 056007–056007 (2013).

27. K. S. K. Wong, Y. Jian, M. Cua, S. Bonora, R. J. Zawadzki, and M. V. Sarunic, "In vivo imaging of human photoreceptor mosaic with wavefront sensorless adaptive optics optical coherence tomography," Biomed. Opt. Express **6**, 580–590 (2015).

28. Y. Jian, S. Lee, M. Ju, M. Heisler, W. Ding, R. Zawadzki, S. Bonora, and M. Sarunic, "Lens-based wavefront sensorless adaptive optics swept source OCT," Sci. Rep. **6**, 27620–27620 (2015).

29. H. R. G. W. Verstraete, S. Wahls, J. Kalkman, and M. Verhaegen, "Model-based sensor-less wavefront aberration correction in optical coherence tomography," Opt. Lett. **40**, 5722–5725 (2015).

30. A. Gullstrand, "Appendix 2," in "Handbuch der Physiologischen Optik," , H. Von Helmholtz, ed. (Opt. Soc. Am. 1924 **1**, 1909), pp. 351–352, 3rd ed.

31. Y. Le Grand and S. G. El Hage, "Physiological optics," Springer Ser. Opt. Sci. (1980).

32. Y. Jian, K. Wong, and M. V. Sarunic, "Graphics processing unit accelerated optical coherence tomography processing at megahertz axial scan rate and high resolution video rate volumetric rendering," J. of Biomed. Opt. **18**, 026002 (2013).

33. M. P. Chang, A. Zadrozny, D. F. Buscher, C. N. Dunlop, and D. J. Robinson, "Hysteresis correction of a piezoelectrically actuated segmented mirror," in "Astronomical Telescopes & Instrumentation," (International Society for Optics and Photonics, 1998), pp. 864–871.

34. Q. Yang, C. Ftaclas, M. Chun, and D. Toomey, "Hysteresis correction in the curvature adaptive optics system," J. Opt. Soc. Am. A **22**, 142–147 (2005).

35. A. Dubra, J. Massa, and C. Paterson, "Preisach classical and nonlinear modeling of hysteresis in piezoceramic deformable mirrors," Opt. Express **13**, 9062–9070 (2005).

36. Y. Qin, Y. Tian, D. Zhang, B. Shirinzadeh, and S. Fatikow, "A novel direct inverse modeling approach for hysteresis

compensation of piezoelectric actuator in feedforward applications," IEEE/ASME Trans. Mechatronics **18**, 981–989 (2013).

37. R. K. Tyson, *Principles of adaptive optics* (CRC press, 2015).
38. L. Bliek, H. R. G. W. Verstraete, M. Verhaegen, and S. Wahls, "Online optimization with costly and noisy measurements using random Fourier expansions," arXiv:1603.09620v2 [cs.LG] (2016).
39. A. H. Sayed and T. Kailath, "Recursive least-squares adaptive filters," Digit. Signal Process. Handbook pp. 21–1 (1998).
40. M. Cua, S. Lee, D. Miao, M. J. Ju, P. J. Mackenzie, Y. Jian, and M. V. Sarunic, "Retinal optical coherence tomography at 1 μm with dynamic focus control and axial motion tracking," J. Biomed. Opt. **21**, 026007 (2016).
41. R. de Kinkelder, J. Kalkman, D. J. Faber, O. Schraa, P. H. Kok, F. D. Verbraak, and T. G. van Leeuwen, "Heartbeat-induced axial motion artifacts in optical coherence tomography measurements of the retina," Invest. Ophthalmol. Vis. Sci. **52**, 3908–3913 (2011).
42. M. J. Booth, "Wave front sensor-less adaptive optics: a model-based approach using sphere packings," Opt. Express **14**, 1339–1352 (2006).
43. J. Antonello, M. Verhaegen, R. Fraanje, T. van Werkhoven, H. C. Gerritsen, and C. U. Keller, "Semidefinite programming for model-based sensorless adaptive optics," J. Opt. Soc. Am. A **29**, 2428–2438 (2012).
44. M. Pircher, B. Baumann, E. Götzinger, H. Sattmann, and C. K. Hitzenberger, "Simultaneous slo/oct imaging of the human retina with axial eye motion correction," Opt. Express **15**, 16922–16932 (2007).
45. C. K. Sheehy, Q. Yang, D. W. Arathorn, P. Tiruveedhula, J. F. de Boer, and A. Roorda, "High-speed, image-based eye tracking with a scanning laser ophthalmoscope," Biomed. Opt. Express **3**, 2611–2622 (2012).
46. T. Klein, W. Wieser, C. M. Eigenwillig, B. R. Biedermann, and R. Huber, "Megahertz OCT for ultrawide-field retinal imaging with a 1050nm fourier domain mode-locked laser," Opt. Express **19**, 3044–3062 (2011).
47. D. Wilding, P. Pozzi, O. Soloviev, G. Vdovin, C. J. Sheppard, and M. Verhaegen, "Pupil filters for extending the field-of-view in light-sheet microscopy," Opt. Lett. **41**, 1205–1208 (2016).

1. Introduction

Since the inception of optical coherence tomography (OCT) in 1991 [1], it has contributed to significant advancements in clinical ophthalmic imaging. A particular strength of OCT is the ability to visualize the cross-sectional thickness of the retina, and the various cell layers that are organized by function. With the axial resolution dependent on the coherence length, but decoupled from the optics delivering light to the eye, commonly available OCT systems were designed to have a depth of focus that encapsulated the entire retinal thickness. This design goal is commonly achieved using of a probe beam diameter of ~1 mm incident on the cornea, resulting in a focused spot size of ~20 μm at the retina. In order to reveal the cellular structures of the retina, such as the cone photoreceptor mosaic and the nerve fibre bundles, the resolution of the imaging system needs to be increased. Given the fixed focal length of a representative eye, the focal waist can be reduced by imaging with a larger beam at the pupil. In the special case of healthy volunteers with good eye optics, OCT imaging systems are capable of imaging parafoveal or perifoveal photoreceptor cones [2–4]. However, the image reliability and quality of the cone photoreceptor images deteriorate when imaging with a large incident beam because of wavefront aberrations present in the refractive elements of the eye.

For the majority of eyes, Adaptive Optics (AO) is essential to maximize the image quality for *in vivo* optical retinal imaging with a large pupil [5]. In particular, this is true for resolving the cone mosaic close to the fovea, where the cone photoreceptor density increases, as the diameter of the cones dercease to ~2 μm in the center of the fovea. Adaptive optics OCT has been reported to improve the quality of *in vivo* retinal images to such an extent that single cone photoreceptors and individual nerve fiber bundles are clearly resolved [6–12]. Conventional AO-OCT imaging systems use a Shack-Hartmann (SH) wavefront sensor to directly quantify and reconstruct the ocular wavefront aberrations. An active component such as a deformable mirror or lens is then used to remove these aberrations. The image quality obtained with these systems are excellent. However, AO-OCT systems containing wavefront sensors are susceptible to wavefront reconstruction errors. If back-reflections and non-common path errors are not properly taken into account, they can lead to poor performance in the wavefront reconstruction [13]. Limitations of the SH wavefront sensor based AO systems occur in cases where subjects have irregularly shaped

pupils, cloudy corneas, or other ocular opacities that scatter light back to the SH wavefront sensor, obscuring the detection of the ocular aberrations. Additional reasons for removing the wavefront sensor out of an AO system are to reduce the size, complexity, and cost of the AO system. These drawbacks of the SH wavefront sensor have led to the development of wavefront sensorless AO (WFSL-AO) algorithms.

In place of a direct measurement of the optical aberrations, WFSL-AO algorithms attempt to remove the optical aberrations by optimizing an image quality metric based on a sequence of images acquired with different test aberrations applied to the adaptive element [14–18]. Implementations of WFSL-AO for retinal imaging with scanning laser ophthalmoscopy (SLO) have been demonstrated using metrics determined by the brightness or sharpness of an image [19, 20]. WFSL-AO OCT was first demonstrated with a simulated annealing optimization algorithm [21]. A coordinate search (CS) algorithm was also demonstrated to improve the OCT signal [22, 23]. More recently, *in vivo* WFSL-AO OCT has been demonstrated for retinal imaging of mice [24–26] and humans [27, 28], also using a CS algorithm.

A limitation of the CS algorithm for *in vivo* imaging is that it is susceptible to noise (i.e. motion artifacts) in the data used for the quality metric during the optimization process. In mice and especially in human subjects, involuntary eye movements such as microsaccades, tremor, and drift can significantly degrade the OCT volumes by causing motion artifacts. If the noise artifact causes the CS algorithm to select an improper coefficient for a particular Zernike mode, the algorithm cannot recover. For robust *in vivo* imaging with WFSL-AO, an image quality optimization algorithm that accounts for motion artifacts is essential.

The Data-based Online Nonlinear Extremum-seeker (DONE) algorithm was first described for WFSL-AO in OCT [29]. In contrast to the aforementioned algorithms that take the measurement with the lowest (or highest) metric value, DONE was explicitly designed to take all past measurements into account such that the robustness of the algorithm with respect to noise is increased. Figure 1 shows an example of optimization performed with the DONE algorithm generalized to a one dimensional case. Instead of assuming a convex merit function (solid line), the DONE algorithm fits a random cosine model to the measurements (dashed line). With every new metric evaluation, the DONE algorithm updates the random cosine model of the merit function, improving its robustness with respect to noisy measurements.
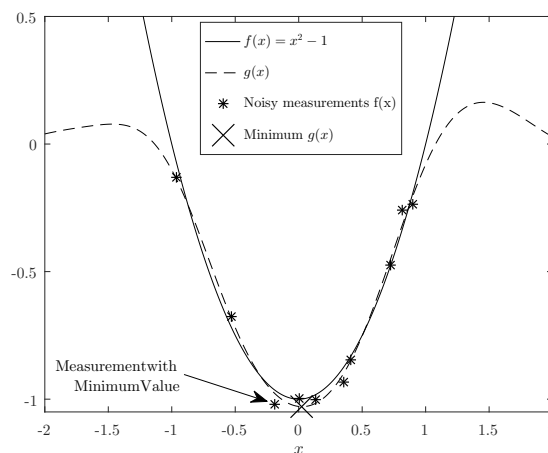

Fig. 1. Example of optimization with DONE. The unknown function $f(x)$ is approximated by the random cosine model $g(x)$ with ten noisy measurements. The minimum of $g(x)$ is found and approximates the minimum of $f(x)$.

The purpose of this report is to demonstrate the DONE algorithm for *in vivo* retinal imaging in humans with WFSL-AO OCT. Our choice of wavefront correcting element was the multi-actuator adaptive lens (MAL), described and demonstrated for mouse retinal imaging in [25]. An advantage of a transmissive adaptive lens is that it can be more readily integrated with a wide range of existing imaging systems by placing it in existing pupil planes, unlike a conventional deformable mirror, which requires optical setups to relay the pupil plane with folded optical paths [25]. The MAL was recently demonstrated for WFSL-AO OCT for human retinal imaging in a compact system using a CS algorithm [28]. However, the CS algorithm was sensitive to motion during the optimization process. Furthermore, the piezoelectric actuators in the MAL suffer from hysteresis, which was compensated by adding additional steps into the CS optimization algorithm in [28], increasing the time required for optimization.

This paper demonstrates that the DONE algorithm can be used for WFSL-AO OCT for *in vivo* human retinal imaging using an adaptive lens as the wavefront corrector. When performing *in vivo* imaging, high speeds are imperative for both image acquisition, as well as computation of the optimization algorithm. To meet the necessity of high speed imaging, we implemented a high speed DONE routine to calculate the random cosine model between the successive OCT volume acquisitions of the optimization process. In order to more accurately determine the wavefront aberration introduced by the lens, the hysteresis effect of the actuators was characterized, and then suppressed during *in vivo* optimization to increase the accuracy of the MAL without the presence of a wavefront sensor for feedback. We present WFSL-AO OCT images acquired in human subjects, that are not trained in visual fixation, and demonstrate successful aberration correction even in the presence of motion artifact.

2. Materials and methods

The measurements were performed with a compact clinical WFSL-AO OCT system described in [28] which contained two deformable transmissive optical elements. For convenience, the optical layout of the system is presented in Fig. 2. The light source used for imaging was a double buffered 200 kHz effective line rate swept source laser (1060 nm center wavelength, 80 nm FWHM bandwidth, instantaneous coherence length specified as 6.3 mm, Axsun, Inc.). The results of a Zemax simulation of the lens-based sample arm, shown in Fig. 2, indicated that the optical design was diffraction limited over a 1.5° scan range. The wavefront aberrations of the optical configuration were experimentally measured to be ~0.069 nm RMS, which is below the Maréchal criterion for diffraction limited imaging (wavelength divided by 14). The first deformable lens was a MAL with 18 actuators described in more detail in [25], placed adjacent to the collimator. The MAL was capable of generating Zernike modes up to the fourth order, but the maximum aberration size for the higher order aberrations was limited. The MAL was used to adjust fine focus, the vertical and oblique astigmatisms, and either two comas or two trefoils. The pupil plane was related to the second deformable lens, which was a variable focal length lens (Varioptics ARCTIC 316-AR850) and was used to manually correct the bulk of the defocus in the human eye. The beam size on the subject's pupil had a Gaussian profile with a $1/e^2$ diameter of 4.8 mm. The calculated $1/e^2$ waist was ~2.4 μm based on Gaussian beam calculations using the Gullstrand-LeGrand model of the human eye [30, 31]. Real-time processing of the OCT data was done on a GPU as described in [32].

2.1. Hysteresis correction of the multi-actuator adaptive lens

The MAL has 18 piezoelectric actuators that suffer from hysteresis. The hysteresis error of a single actuator is approximately 14%. In order to achieve the maximum possible accuracy in depicting optical wavefront aberrations with the MAL without using a wavefront sensor, the hysteresis was characterized and compensated. Several methods exist to correct hysteresis in deformable mirrors, for example [33–35]. This information was used to linearize the response
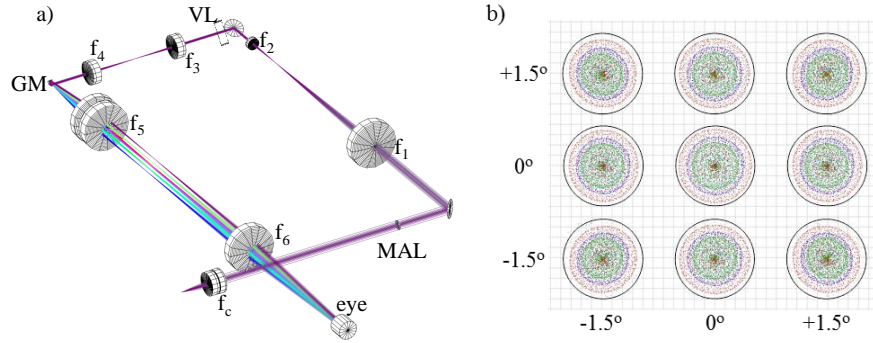
Fig. 2. (a) Zemax 3D simulation of the lens-based sample arm. (b) Spot diagram for three wavelengths spanning the 80 nm bandwidth of the light source (green, 1020 nm; blue, 1060 nm; red, 1100 nm). The eye was modeled as a paraxial lens with 16 mm focal length in air. VL, location of variable focus lens; GM, galvo scanning mirrors. Lenses: f_c, 37.5 mm; f_1, 200 mm; f_2, 50 mm; f_3, 50 mm; f_4, 50 mm; f_5, 100 mm; f_6, 200 mm.

of the piezoelectric actuators in terms of the voltage input and displacement. The method used for hysteresis correction directly approximated the inverse hysteresis curve with a combination of a polynomial and a Prandtl-Ishlinskii (PI) model [36]. The model used was formed by the discrete-time elementary backlash operator and a polynomial:

$$H_r[S(\bar{u})](t) = \max\{S(\bar{u}(t)) - r, \min\{S(\bar{u}(t)) + r, H_r[S(\bar{u})](t - T)\}\}, \qquad (1)$$

where $\bar{u}(t)$ is the input, r is the threshold, a sampling time T is used, and the polynomial $S(\bar{u}(t)) = c_m \bar{u}^m(t) + c_{m-1}\bar{u}^{m-1}(t) + \cdots + c_1\bar{u}^1(t)$. Assuming that the piezoelectric actuators started from the de-energized state, the initial condition $H_r[S(\bar{u})](0)$ was set to zero. The full model was then expressed as

$$\bar{\phi}^{-1}(\bar{u}(t)) = \sum_{i=1}^{n} w_i H_{r_i}[S(\bar{u})](t). \qquad (2)$$

The weights w_i were fitted to match the model to the inverse hysteresis curve. The number of backlash operators was set to $n = 40$, the order of the polynomial was set to $m = 7$, and the thresholds $r_i = 0.02(i - 1)$. We fitted the hysteresis according to the following procedure. A Shack-Hartmann (SH) wavefront sensor was placed at a conjugate plane of the MAL such that the influence matrix of the lens could be measured. Each of the 18 piezoelectric actuators of the MAL were then sequentially actuated and the change in wavefront error was recorded by the SH sensor. The procedure was repeated separately for each actuator. Figure 3 shows a measured hysteresis curve identifying the relationship $y(t) = \phi(u(t))$ between the input $u(t)$ of one actuator of the MAL and the normalized change in the wavefront error $y(t)$. The inverse ϕ^{-1} of this measured hysteresis curve was approximated by $\bar{\phi}^{-1}$, a PI model combined with a polynomial fit. Assuming that the real input of the actuator was set to $u(t) = \bar{\phi}^{-1}(\bar{u}(t))$, then the model of the inverse hysteresis function was used to derive an input for the actuator that resulted in a linear relationship between the wavefront error and the linear desired input of the actuator $\bar{u}(t)$, $y(t) = \phi(\bar{\phi}^{-1}(\bar{u}(t))) \approx \bar{u}(t)$. The linear realization can be seen in Fig. 3. Using our approach the maximum hysteresis error after the linearization was below 2%. The procedure was repeated for all actuators. After linearization, the response of all actuators of the lens was considered to be linear. This resulted in an influence matrix that is valid over the entire stroke of the MAL and turns the generation of arbitrary wavefront aberrations into a linear problem [37]. The normalized
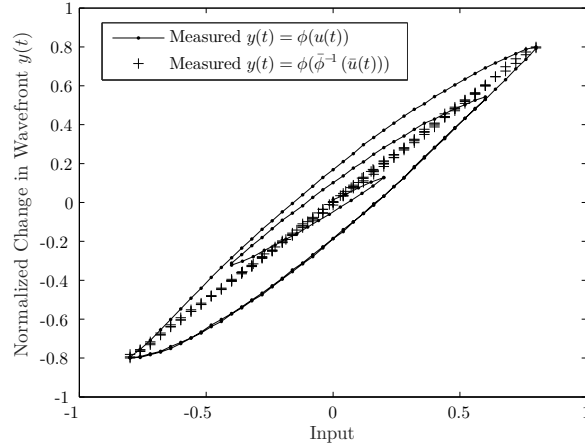
Fig. 3. Hysteresis curve of piezoelectric actuator measured by Shack-Hartmann wavefront
sensor before and after linearization.

Zernike coefficients depicted on the MAL can be calculated as $\mathbf{x} = \mathbf{M}\bar{\mathbf{u}}$, where $\mathbf{M}$ is derived
from the influence matrix and $\bar{\mathbf{u}} = [\bar{u}_1, \bar{u}_2, \ldots, \bar{u}_{18}]^T$ is a vector of the desired linear inputs of
all 18 actuators. The calibration for the linearization of the actuators was performed once and
remained stable for all of the following imaging experiments.

2.2.   The DONE algorithm

For the application of WFSL-AO OCT to *in vivo* human retinal imaging, minimization of the
optimization time is essential to reduce the effects of motion artifact on the aberration correction
process. In order to perform the DONE model computations in near real-time, fast algorithms are
necessary. We present an improved and faster implementation of the DONE algorithm [29, 38]
used to maximize the AO-OCT signal for human retinal imaging. The biggest difference between
the DONE algorithm reported in [29] and the current work is a faster implementation that allows
the exploration and the bounds for each aberration to be set independently. Essentially, DONE
maintains a model based on D random cosines of which the amplitudes are determined by a
linear least squares problem. With the least squares solver implementation reported in [29], the
computational time per iteration of the DONE algorithm was ~60 ms. For 70 iterations, the
time for computation alone would exceed 4 s. Hence, we changed the least squares routine
of the DONE algorithm into a recursive procedure, which resulted in a significant increase in
computational speed. With the implementation of the recursive routine, the time per iteration of
the DONE algorithm was reduced to ~1 ms, which is smaller than the settling time of the MAL.

   A pseudocode description of the DONE algorithm was presented in [38]. In iteration n of
DONE, we define $\mathbf{a}_n = \cos(\omega^T \mathbf{x}_n + \mathbf{B})$, where the vector $\mathbf{x}_n$ contains the coefficients of the
Zernike aberrations of the MAL and y_n is the corresponding OCT signal metric value. Moreover,
the matrix ω consists of d by D independent and identically distributed (i.i.d) random frequencies
drawn from a normal distribution with zero mean and standard deviation σ and the column
vector $\mathbf{B}$ consists of D i.i.d phase offsets with values between 0 and 2π drawn from a uniform
distribution. Also, the cos function operates element-wise on a vector. We implemented the
inverse QR algorithm [39, Sec. 21] for the recursive update, which is known to be especially
numerically reliable. The initial amplitudes of the cosines are set to $\mathbf{c}_0 = 0$ and the initial matrix
$\mathbf{P}_0 = \lambda^{-1}\mathbf{I}_{D\times D}$, where λ is the regularization parameter and $\mathbf{I}_{D\times D}$ is an identity matrix with D
columns. We find a rotation matrix $\mathbf{\Theta}_n$ that lower triangularizes the upper triangular matrix in

Eq. (3) below and generates a post-array with positive diagonal entries:

$$\left[\begin{array}{cc} 1 & \mathbf{a}_n^T \mathbf{P}_{n-1}^{1/2} \\ \mathbf{0} & \mathbf{P}_{n-1}^{1/2} \end{array} \right] \mathbf{\Theta}_n = \left[\begin{array}{cc} \gamma_n^{-1/2} & \mathbf{0} \\ \mathbf{g}_n \gamma_n^{-1/2} & \mathbf{P}_n^{1/2} \end{array} \right].$$ (3)

The rotation matrix $\mathbf{\Theta}_n$ can be found by performing a QR decomposition of the transpose of the matrix on the left hand side of (3), or by the procedure explained in [39, Sec. 21]. Then we update the amplitudes of the cosines $\mathbf{c}_n$ as follows,

$$\mathbf{c}_n = \mathbf{c}_{n-1} + \mathbf{g}_n(y_n - \mathbf{a}_n^T \mathbf{c}_{n-1}).$$ (4)

One OCT metric evaluation takes place per iteration and is used to update the model. The model is then defined as $g(\mathbf{x}) = \mathbf{c}_n^T \cos(\omega^T \mathbf{x} + \mathbf{B})$. After the model update, the minimum or maximum of the model $g(\mathbf{x})$ is found. At the end of each iteration the DONE algorithm proposes new values of the Zernike coefficients $\mathbf{x}_{n+1}$ to add on the MAL and the next measurement for the OCT signal metric y_{n+1} is taken. This process is repeated until the algorithm has converged up to a pre-defined maximum number of iterations.

DONE can deal with arbitrary aberrations and is mainly limited by the correction capabilities of the MAL. DONE does not have a predetermined search pattern and will change the position of the measurements based on past metric evaluations. Therefore, the final accuracy of the aberration correction of the DONE algorithm is not limited by the step size as for example compared to the CS algorithm [29]. To improve the accuracy of the lens, hysteresis compensation of the actuators in the lens was necessary. Also, by choosing a small standard deviation for the frequencies of the cosines, the model will serve as a low-pass filter for the metric evaluations, while other algorithms often take the argument of the highest or lowest value of the evaluated metric, which can yield an outlier due to noise as shown in Fig. 1. In this way, DONE mitigates the noise effects of motion on the merit function during the optimization.

2.3.   Human imaging and aberration correction

The performance of DONE in combination with the MAL was investigated by imaging the retinal photoreceptor layer of 10 healthy volunteers with refractive errors of less than 4 diopters. The mean age of the volunteers was 28.3 ± 7.6 years, consisting of 2 females and 8 males. The mean axial length and cylindrical refractive error of the research volunteers (measured with an IOL Master 500) was 24.19 ± 0.94 mm and 1.042 ± 0.52 D respectively. Human retinal imaging was performed in accordance with the research ethics approved by the Office for Research Ethics (ORE) at Simon Fraser University, the University of British Columbia, and Vancouver General Hospital. Written and informed consent was obtained prior to imaging from all imaging subjects. The average power of light incident on the cornea during imaging was limited to 900 μW. Imaging was initiated with the eye dilated, and the subject seated comfortably with their head supported by a chin and forehead rest. An additional benefit of the pupil dilation was that it caused temporary paralysis of the eye's ciliary muscles, preventing accommodation. Prior to the optimization, the subject's eye was aligned to the imaging system and an OCT volume of 400 by 400 A-scans was acquired (pre-optimization). For the optimization procedure, small volumes (C-scans) consisting of 8,000 A-scans (400 × 20) were acquired at a 200 kHz line rate, corresponding to a volume acquisition rate of ∼ 25 volumes per second. *En face* images of the operated selected retinal layer were extracted from the OCT volume in real-time during the optimization. The brightness of the *en face* OCT images was used as the signal metric for the DONE algorithm [23]. The axial position of the retinal layers in the OCT B-scan was dynamically tracked by the acquisition software [40] to account for the axial motion of the subjects [41] and ensure the OCT signal metric was calculated based on the same retinal layer throughout the optimization process. Different retinal layers could be chosen to perform the optimization,

as shown in [28]. In this work we tracked and imaged the photoreceptors in the outer retina. The DONE algorithm was configured to take 70 metric evaluations for the optimization, which corresponded to a total time for the optimization (including actuation of the lens and processing of the small C-scans) of ~3 seconds. Immediately after the optimization a large volume of 400 by 400 A-scans was acquired for the final image (post-optimization).

For human eye imaging, the MAL was used to correct $d = 5$ Zernike aberrations, namely, the defocus, two astigmatisms, and two comas. The empirically determined parameters used for the DONE algorithm optimization in the human eye are described in Table 1. Setting the number of cosines to $D = 1,000$ provided good results for at least up to seven aberrations [29]. The standard deviation of the frequencies of the cosines was $\sigma = 1$, which was set to match the frequency content in the transfer function of the aberration [23]. The regularization parameter $\lambda = 5$ prevented over-fitting of the model. The upper and lower bound vectors **ub** and **lb**, respectively, consisted of the individual bounds for each aberration and matched the maximum capabilities of the lens with hysteresis correction. The vectors σ_η and σ_ξ determined the amount of exploration done by the DONE algorithm for each aberration. The exploration parameters define a trade-off between the number of steps used exploring and the final accuracy, a larger value could result in faster convergence, while a smaller value could lead to a smaller wavefront error. The exploration factor for the comas was set lower than for the other aberrations because the upper bounds of the comas are lower.

Table 1. Parameter values for the DONE algorithm (wavefront aberrations in μm)

DONE	
D	1000
σ	1
λ	5
σ_η, σ_ξ	$[0.07, 0.07, 0.07, 0.025, 0.025]$
ub	$[1.8, 2, 2, 0.4, 0.4]$
lb	$-$**ub**

3. Results

The imaging performance of the DONE algorithm was compared against the hill climbing CS algorithm used in previous work reported using the MAL [24, 28]. In order to provide a comparison between the two optimization techniques, we imaged a tissue phantom with no motion artifact. The DONE algorithm used for phantom imaging was the same as that described for human imaging in the previous section. The CS algorithm was implemented as in the previous work using the MAL [24, 28], using a static look-up-table for the actuator voltages to generate a specific amplitude of a particular Zernike mode. For each Zernike mode, 10 OCT volumes were acquired with the aberration applied to the MAL using coefficient values that were uniformly distributed across the same range of upper and lower bounds (**ub** and **lb**) as used for the DONE algorithm optimization. The coefficient resulting in the highest value of the merit function was selected as the optimized value for that Zernike mode, and applied to the MAL. Subsequent Zernike modes used the optimized values of the preceding modes as the starting point. Because the CS algorithm did not take into account the hysteresis of the lens, the actuators were de-energized by applying a decreasing sinusoid to each of the actuators; this 'relax' procedure required ~100 ms. The CS was performed by relaxing the MAL, applying the previously found optimized values, and then stepping through look-up-table of coefficients. For each Zernike mode, the procedure first searched the positive coefficient values, relaxed the MAL actuators,

and then searched the negative coefficient values. A Shack-Hartmann wavefront sensor placed at the pupil position of the sample arm (optically conjugated to the MAL) was used to measure the interaction of the Zernike modes while running the CS algorithm; the measurements are presented in Visualization 1. The video results indicate that the Zernike modes have been generated by the MAL with minimal cross-talk to the other modes with the exception of coma, and even in that case the effects on the reconstructed wavefront map were minimal. The results of the DONE and CS optimization on a phantom (lens paper fibres) are presented in Fig. 4. The sequences of *en face* images acquired during the optimization process for CS and DONE are presented in Visualization 2. A more elaborate explanation of the results seen in Fig. 4 can be found in the Discussion.
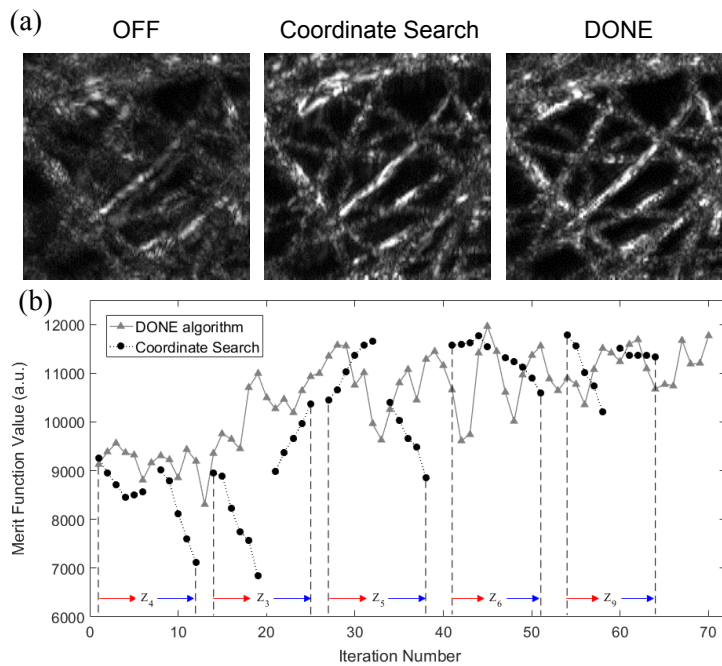

Fig. 4. Comparison of Coordinate Search (CS) and DONE optimization on a stationary sample. (a) Unoptimized and final images of the phantom after aberration correction with the CS and DONE algorithms. (b) Merit function versus iteration for CS and DONE.

3.1. Imaging human photoreceptors

Images of human retina acquired from the research subjects are presented before and after optimization with the DONE algorithm. The images were processed identically. In Fig. 5, a 450 μm by 450 μm *en face* image shows the retinal cones of a healthy subject centered at approximately 3 degrees from the center of the fovea.The *en face* image was extracted from 400 by 400 A-scans. In the pre-optimization image, the individual cones are not resolvable. The contrast and structure of the cones is improved after the optimization; a mosaic pattern can be visualized, and the cones are readily distinguished. The cones are still slightly deformed (non-circular), mainly due to motion artifact and the remaining higher order aberrations.

In Fig. 6, the OCT image metric values are plotted against the iteration number of the DONE algorithm for the optimization used in Fig. 5. The fluctuation of the metric is caused by noise, changing aberrations on the MAL and small movements of the subject's eye. The progress of the metric function during the optimization shows a large increase after the optimization. The

WFSL-AO OCT signal was maximized at the IS-OS junction layer, which becomes 7 times higher after the optimization (from an initial value of 553 to a final value of 3,761). The total root mean square (RMS) wavefront error of the corrected wavefront aberrations was 1.22 μm with an oblique astigmatism that had a RMS wavefront error of 0.53 μm.

The WFSL-AO optimized images from another representative research subject are presented in Visualization 3. Although the focus was optimized at the photoreceptor layer, the full thickness of the retina can be visualized in the OCT volume (post DONE optimization, single acquisition, not averaged). The images presented in the previous figures were acquired on research subjects that had relatively good fixation. Figure 7 shows the optimization of the OCT signal in a different subject who was not trained at fixating their gaze to reduce eye motion. This data demonstrates DONE's ability to function when the subject is not able to maintain a fixed gaze, as suggested from the large motion artifacts that are present both before and after optimization. These motion artifacts, which appear as discontinuities in the *en face* images, are caused by involuntary movements of the subject's eye and are taken into account by the DONE algorithm as noise. A similar improvement in image quality was observed despite the presence of the motion artifacts. Here, the total RMS wavefront error of the corrected wavefront aberrations was 0.58 μm, including a vertical astigmatism with a RMS wavefront error of -0.49 μm.

We investigated the utility of the DONE algorithm optimization for imaging wider regions in the retina. In Figure 8, 12 WFSL-OCT volumes were acquired and manually aligned to generate a montage image. The different regions were acquired by asking the research subject to change the fixation to calibrated points in the field of view. In the central square, the foveal cones are not resolved. The four regions immediately surrounding the central square are presented on a larger scale, demonstrating that the cone photoreceptor mosaics are clearly resolved outside the fovea. Since the size of the cone photoreceptors increases and the cone density decreases at larger eccentricities, the remaining images are also readily resolved.

Before Optimization   After Optimization

Nerve fiber layer
Ganglion cell layer
Inner plexiform layer
Inner nuclear layer
Outer plexiform layer
Outer nuclear layer
External limiting membrane
IS/OS junction
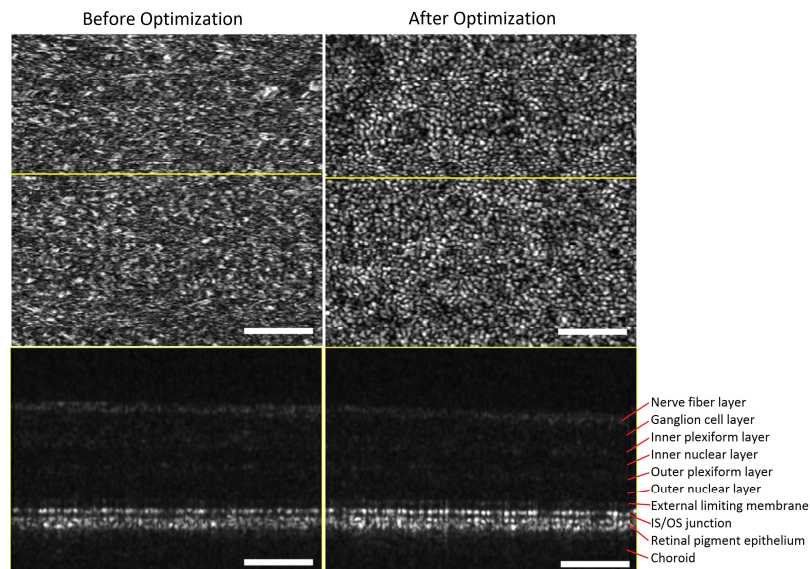Retinal pigment epithelium
Choroid

Fig. 5. The top row shows the OCT *en face* image of human photoreceptors before and after optimization using 70 iterations of DONE. The bottom row shows the corresponding B-scans at the location shown in yellow on the *en face* image. All scale bars are 100 μm. The optimized Zernike coefficients (in μm): Defocus, -0.94; Oblique Astigmatism, 0.53; Vertical Astigmatism, -0.069; Vertical Coma, 0.40; Horizontal Coma, 0.40.
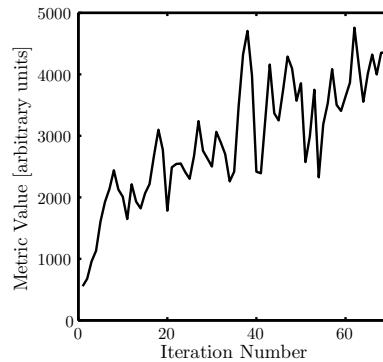
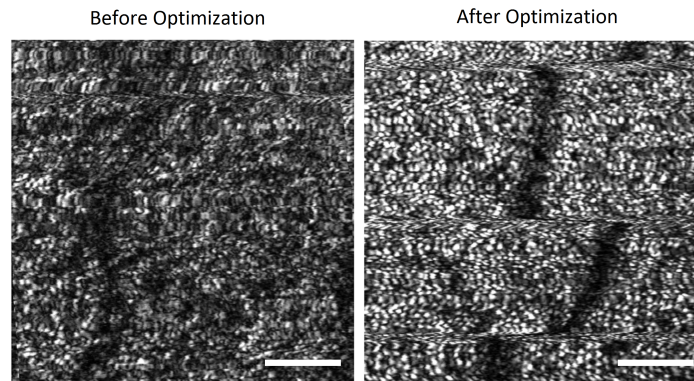Fig. 6. Values of the metric function during the optimization with the DONE algorithm.

Fig. 7. OCT *en face* image of human photoreceptor starting before and after optimization with 70 iterations of DONE. All scale bars are 100 μm. The optimized Zernike coefficients (in μm): Defocus, 0.25; Oblique Astigmatism, -0.16; Vertical Astigmatism, -0.49; Vertical Coma, -0.059; Horizontal Coma, -0.11.

4. Discussion

We demonstrated WFSL-AO OCT aberration correction using the DONE algorithm and a multi-actuator adaptive lens (MAL) for human retinal imaging *in vivo*. This work represents the results of an international collaboration, and relative to our previous works, a significant advance towards WFSL-AO OCT imaging with a MAL in a clinical setting. In terms of the system hardware, the non-linearity and hysteresis of the MAL was removed. Algorithmically, an improved version of the DONE algorithm was developed and implemented to minimize the computational time required in between data points. In combination, the linearized lens and the high-speed DONE algorithm were used to maximize the WFSL-AO OCT signal from the human retina in different subjects. The linearization of the hysteresis did not need to be repeated for the measurements of the ten subjects. Physical changes in the lens may cause a slow variation of the hysteresis fit, however, our results demonstrated that they remained valid during the entire period of data acquisition of all subjects. Similar to the linearization of the MAL actuators, the tuning of the parameters of the DONE algorithm was done beforehand.

The results acquired on the tissue phantom in Fig. 4 demonstrated that the DONE algorithm and the CS algorithm arrived to very similar results for the optimization of a static sample. The CS algorithm did not have hysteresis compensation, and required a 'relax' procedure, which
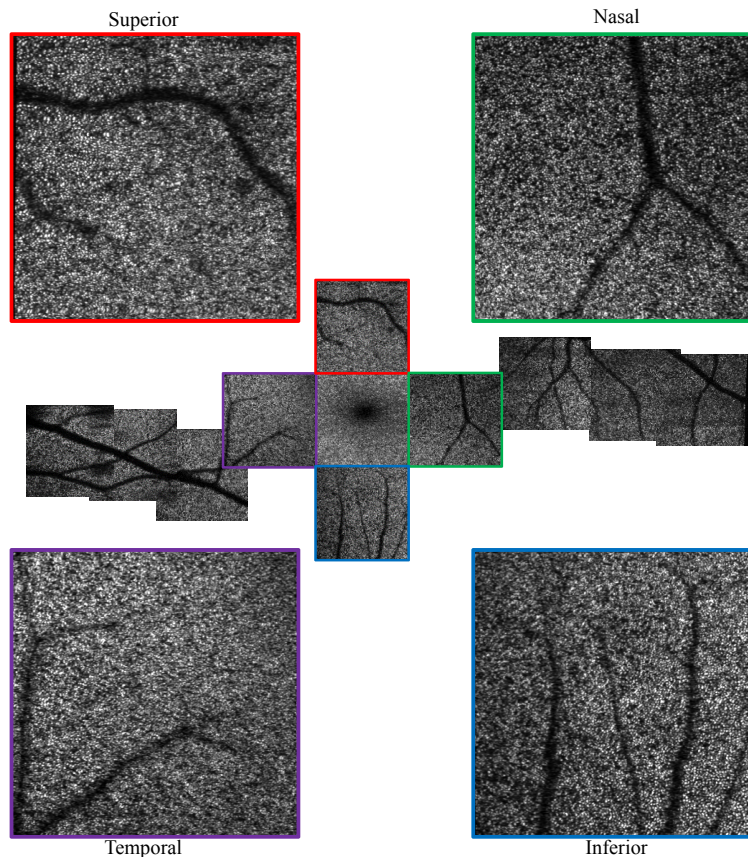
Fig. 8. Mosaicked images of the retina acquired across a retina in a single imaging session. The position on the retina was controlled by asking the subject to fixate on different calibrated points in the visual field.

added significantly to the optimization time. A key difference between the CS and DONE algorithms is apparent in the graph of merit function versus iteration number in Fig. 4 (b). The merit function measurements for the CS algorithm showed significant variations when scanning through each Zernike mode. A small motion artifact affecting the CS early in the optimization process could have disastrous results on the overall result, causing the selection of an incorrect value for a Zernike mode coefficient because of noisy outliers. In contrast, the merit function measurements for the DONE algorithm show a general upward trend, and due to the model fitting on the past measurements, is more resistant to the noise in the measurements.

Model based algorithms for WFSL-AO converge faster than stochastic approaches [29, 42, 43]; taking into account prior knowledge of the optical system to reduce the required number of measurements for the optimization [42, 43]. However, in retinal OCT imaging, the use of a static model of the refractive elements of the eye, the cornea and intraocular lens, is hampered by of significant variation among subjects. Using information of past measurements in a dynamic model can increase the accuracy and robustness of the optimization algorithm with respect to the noise level of the measurements. In [23] we showed that all wavefront aberrations can be removed in a wavefront sensorless manner by maximizing the signal intensity in an OCT system.

When comparing the images of the retina before and after optimization in Fig. 5, the images after wavefront correction show more contrast. The increase of the image quality metric shown

in Fig. 6, which is the average WFSL-AO OCT signal at the IS-OS junction layer, confirms an increase in the OCT signal by a factor seven and, hence, an improvement in the signal to noise ratio. When comparing the images before and after optimization in Fig. 5 and Fig. 7, the images after wavefront correction clearly show that features such as the cones and blood vessels are sharper and have more contrast after optimization. Additionally, it should be noted that not only the intensity of the WFSL-AO OCT signal of the cones improves, but also the shape becomes more circular.

The DONE parameters are general for human retinal imaging with the MAL and the number of aberrations corrected, and were kept constant for all the measurements reported. The results demonstrate that the DONE algorithm has successfully corrected aberrations during *in vivo* measurements, which resulted in improved WFSL-AO OCT images. The circumstances under which the optimization algorithm has to perform have become clearer from the data acquisition. In Fig. 7 motion artifacts show small lateral movements of the eye within the C-scan. Throughout the optimization the sample is continuously moving by similar amounts and the metric was evaluated at slightly different lateral locations. The DONE algorithm was exhibited to be robust with respect to unexpected motion induced noise in the image quality metric. Further improvements to the optimization algorithm can be made by filtering out measurements when the signal disappears due to big movements of the eye. However, if relatively long lasting signal deviations that can no longer be considered noise occur, like blinking, the DONE algorithm could fail to find an improved WFSL-AO OCT signal.

Mitigation of the motion artifact during optimization is essential for successful aberration correction with WFSL-AO OCT. Eye movements and blinking are more likely to occur if the duration becomes too long, which in turn will deteriorate the performance of the algorithm. However, as mentioned previously, the minimum number of iterations permitted will also impact the performance. Active tracking of eye movements could reduce the movement of the image [44, 45], but it would lead to additional hardware and added costs for implementation. Fast optimization methods are imperative for application of WFSL-AO aberration compensation to a large group of people. The rate limiting factor of the present WFSL-AO OCT implementation was the time for acquisition of the OCT volumes with a 200 kHz A-scan light source (nominally 40 ms). However, with a state-of-the-art 1.5 MHz Fourier domain mode locking source [46], the volume acquisition time could be reduced to ~5 ms. The second limiting factor of the current implementation was the settling time of the MAL, which was on the order of 5 ms. In this report, we presented a recursive implementation of the DONE algorithm with a computational time of only one millisecond per iteration. For the number of iterations performed in this report, and with incremental modifications to the system, the optimization speed could be in the order of a second with the current set of search parameters for the DONE algorithm.

The aberration correcting performance of DONE relative to the CS was previously presented in [29]. For trained fixators with normal eyes, there were no significant differences in the final image quality with DONE or with the CS algorithm. Empirically, our experience was that the DONE algorithm was more reliable in terms of obtaining an aberration correction for subjects with an average gaze fixation ability. This is emphasized in the graph of Fig. 6. The value of the metric function trends upwards even in the presence of motion artifact induced noise in the measurements.

The number of iterations used in the DONE algorithm is a trade-off between the amount of time available for searching, and the final aberration corrected performance. Whenever considering more wavefront aberration modes to correct, more measurements are needed. In contrast, the parameters of the DONE algorithm will remain largely the same, even for more modes. The maximum stroke of the MAL limits the maximum amplitudes of the modes, hence the exploration parameters and bounds for each mode should be carefully chosen. Previously, DONE has successfully been used in WFSL-AO OCT, light sheet microscopy, and simulations

of an optical beam forming network [29, 38, 47]. It was shown that DONE outperforms other algorithms in residual wavefront error and convergence speed [29].

5. Conclusion

Ophthalmic AO systems with wavefront sensors and deformable mirrors can provide a closed-loop correction at rates of 10 - 100 Hz, correcting multiple large amplitude Zernike aberrations simultaneously and providing continuous correction during imaging. At present, wavefront sensorless aberration correction methods do not reach these levels of performance in ophthalmology, but they already are at a level where retinal image quality can benefit from adaptive optics with low system complexity and cost.

The improved and faster version of the DONE optimization algorithm was demonstrated, achieving a computational time of 1 ms per iteration, making it applicable for many high speed applications in optics. In this report, the DONE algorithm was successfully applied to drastically improve the OCT signal during *in vivo* measurements of the human eye. The optical wavefront aberrations were corrected using a multi-actuator adaptive lens after linearizing the hysteresis of the actuators to improve the accuracy. We have shown that the improved version of the DONE algorithm is fast enough for in vivo retinal imaging and robust towards small involuntary movements of the eye which it considers as noise in the changing OCT signal.